

Time-Resolved TOF MR Angiography in Mice Using a Prospective 3D Radial Double Golden Angle Approach

Aurelien J. Trotier, William Lefrançois, Emeline J. Ribot, Eric Thiaudiere, Jean-Michel Franconi, and Sylvain Miraux*

Purpose: To develop an undersampled anatomical, three-dimensional (3-D) time-resolved magnetic resonance angiography (MRA) method for small animals based on time-of-flight (TOF) effect and radial sampling.

Methods: Mouse carotid arteries and Circle of Willis images were acquired on a 7T scanner with an electrocardiogram (ECG)-triggered sequence. Preliminary experiments were used to generate an approximately uniform distribution of radial projections with a first golden angle and to produce anatomical TOF images. A second golden angle ratio between consecutive projections of cine acquisitions was added to make it possible to use a temporal filter during reconstruction of time-resolved angiography. A decreasing number of projections were tested, and their impact on signal-to-noise ratio (SNR) and spatial resolution was assessed.

Results: In anatomical MRA, the undersampled radial approach efficiently allows fast acquisition of mouse angiogram in 3D (22 sec). It was also only slightly sensitive to motion and flow artifacts. The time-resolved sequence can be performed with only 2,500 projections per cine and a temporal resolution under 4 ms in a relatively short acquisition time (less than 5 min).

Conclusion: This technique simultaneously provided high 3D isotropic spatial resolution and excellent temporal resolution with a good SNR level, allowing blood flow to be visualized in a restricted acquisition time. **Magn Reson Med 000:000–000, 2014. © 2014 Wiley Periodicals, Inc.**

Key words: TOF angiography; 3D radial; time-resolved; golden angle; temporal filter; small animals

INTRODUCTION

Recently, the number of small animal models for the analysis of physiological and pathological anatomy in the field of vascular biology has increased (1–5). To characterize these models, specific noninvasive methods are required. Time-of-flight (TOF) magnetic resonance angiography (MRA), due to its high spatial resolution and the inherent vessel contrast obtained without requiring injection of contrast agent, appears to be a powerful

method (6–9). However, TOF-MRA only provides anatomical information. In humans, it could be very useful to be able to evaluate dynamic flow patterns in a number of vascular applications, such as when assessing collateral circulation in patients with cerebrovascular stenosis (10,11), estimating the degree of blood flow shunted onto the peripheral vasculature (12), or determining abnormal blood flow due to an intracardiac shunt (13). In small animals, it could greatly help to better characterize and to reduce animal variability in numerous models of pathologies, such as hypertension (14,15), atherosclerosis (16), or stroke (17), and to develop efficient therapies against these diseases.

In clinical studies, time-resolved angiography with contrast agent injection was first described in the late 1980s. Initially, the method provided a lower spatial resolution than did static MRA, but it did offer sufficient temporal resolution to assess dynamic vascular phenomena.

Since then, many technical improvements have been made, such as parallel imaging and the use of high-intensity gradient systems (18). These innovations, combined with innovative acquisition and reconstruction strategies of view sharing (19), such as time-resolved imaging of contrast kinetics (TRICKS) (20) or keyhole (21), made it possible to obtain three-dimensional (3D) images every 5 seconds (22). More recently, radial trajectory imaging was shown to be very robust for undersampling (vastly undersampled isotropic projection reconstruction) and to reduce acquisition times 30- to 40-fold (23). Finally, scan time was further reduced by applying highly constrained backprojection (24) or compressed sensing (25) methods. It now is possible to acquire 3D images on humans with a time resolution of less than 1 second and a spatial resolution of 8 mm (26). However, these methods require the use of injected contrast agents. This makes them difficult to perform longitudinally on small animals, and it carries a potential risk for patients who may develop nephrogenic systemic fibrosis (27).

Alternative time-resolved angiography methods not requiring contrast agent injection have thus been investigated. They are based on a cine approach in which it is assumed that the same temporal behavior is repeated for each cardiac cycle. The temporal resolution must be better than that achieved in time-resolved contrast-enhanced imaging. In humans, these methods are based on pseudocontinuous arterial spin labeling (28,29) or balanced steady-state free precession acquisition (30). For small animals, a strategy based on TOF cine imaging after signal suppression was developed (31). These non-enhanced MR sequences have a high temporal resolution (less than 10 ms), and acquisition can be triggered by

Centre de Résonance Magnétique des Systèmes Biologiques, UMR 5536 CNRS/Université Bordeaux Segalen, Bordeaux Cedex, France.

*Correspondence to: Sylvain Miraux, Centre de Résonance Magnétique des Systèmes Biologiques, UMR 5536 CNRS/Université Bordeaux Segalen, 146 rue Léo Saignat, 33076 Bordeaux Cedex, France.

E-mail: miraux@rmsb.u-bordeaux2.fr

Additional Supporting Information may be found in the online version of this article.

Received 18 November 2013; revised 11 February 2014; accepted 11 February 2014

DOI 10.1002/mrm.25201

Published online 00 Month 2014 in Wiley Online Library (wileyonlinelibrary.com).

© 2014 Wiley Periodicals, Inc.

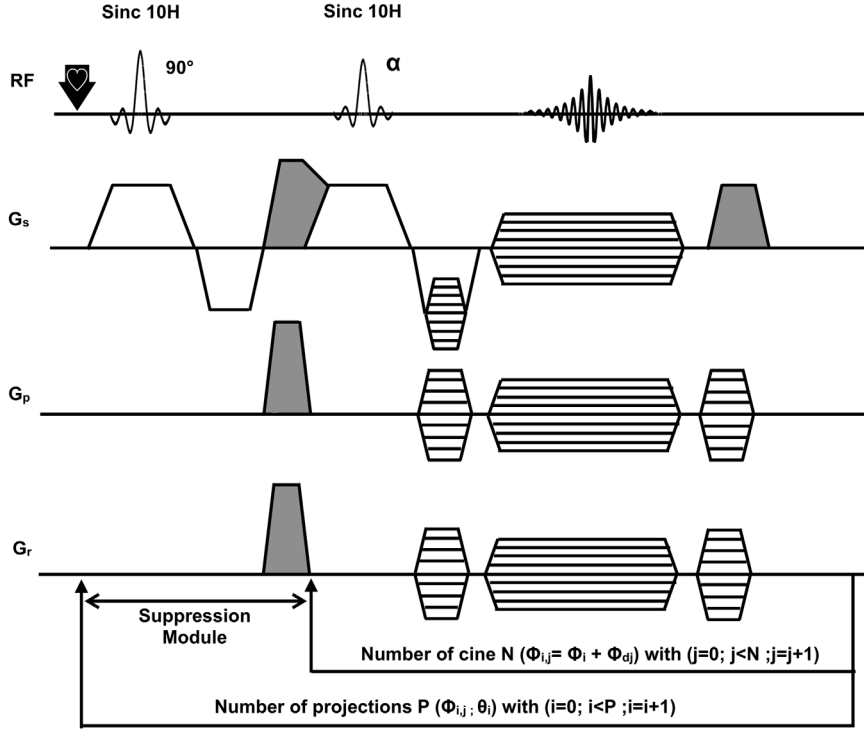


FIG. 1. Timing diagram of the electrocardiogram (ECG)-triggered sequence used for three-dimensional radial bright-blood cine magnetic resonance angiography. A suppression module was added before N-cine images. Each cine image was acquired with P ($\Phi_{i,j}$, θ_i) projections. For each cine image, $\Phi_{i,j} = \Phi_i + \Phi_{\theta j}$, where i is the projection number and j is the cine number. Spoiler gradients are indicated in gray. The black arrow represents the ECG trigger.

electrocardiogram (ECG) (32,33). However, the total acquisition time required to generate 3D images with high spatial and temporal resolutions can be prohibitive. It can be a limiting factor for studies involving large cohorts of animals.

As mentioned above, radial imaging can provide high-quality images with a high undersampling factor. In addition, combining it with a nonconventional golden angle projection scheme makes it possible to obtain flexible spatial and temporal resolutions for retrospectively reconstructed images (34).

To our knowledge, this type of radial imaging approach has never been applied for anatomical and time-resolved TOF MRA.

In this study, we present anatomical TOF images with a high factor of undersampling generated using a first golden angle ratio to produce an approximately uniform distribution of radial projections. A second golden angle ratio was then applied between consecutive projections of an ECG-triggered cine acquisition to increase the spatial resolution of time-resolved undersampled angiography images using a temporal filter. This method was validated on phantom samples and used to image carotid arteries and the Circle of Willis in mice at 7T.

METHODS

Double Golden Angle Approach

3D golden angle radial trajectories

Three-dimensional anatomical TOF imaging is based on the 3D projection of trajectories defined by 2D golden means $v_1 = 0.6823$ radians and $v_2 = 0.4656$ radians. The polar and azimuthal angles, θ and Φ , were defined to

implement the 2D golden means on a hemisphere in the k-space (35):

$$\Phi_i = 2\pi \times \text{mod}(v_1 \times i, 1) \quad [1]$$

$$\theta_i = \text{acos}(\text{mod}(v_2 \times i, 1)) \quad [2]$$

where i is the projection number. In this article, we modified this implementation by adding π to Φ_i for odd values of i . This modification entails initial projections throughout the k-space sphere rather than just on a hemisphere, as defined by Chan et al. (35). In Cartesian coordinates, projections start at the k-space coordinates (k_x , k_y , k_z):

$$k_{x_i} = k_{\text{max}} \times \cos(\Phi_i) \sin(\theta_i) \quad [3]$$

$$k_{y_i} = k_{\text{max}} \times \sin(\Phi_i) \sin(\theta_i) \quad [4]$$

$$k_{z_i} = k_{\text{max}} \times \cos(\theta_i) \quad [5]$$

3D time-resolved radial golden angle

In conventional fast low-angle shot cine sequences, a set of N gradient-echo images was acquired with the same trajectory in the k-space, where N was the cine number.

In our sequence (Fig. 1), each cine consists of P projections defined by golden angles (θ_i ; Φ_i), as previously described.

To enhance spatial resolution with a temporal filter during reconstruction, it is preferable to have different k-space trajectories between cine images. Thus, projections of each cine were defined by the same golden angle trajectories, but an additional polar angle, θ_{dj} , was included for each j^{th} cine:

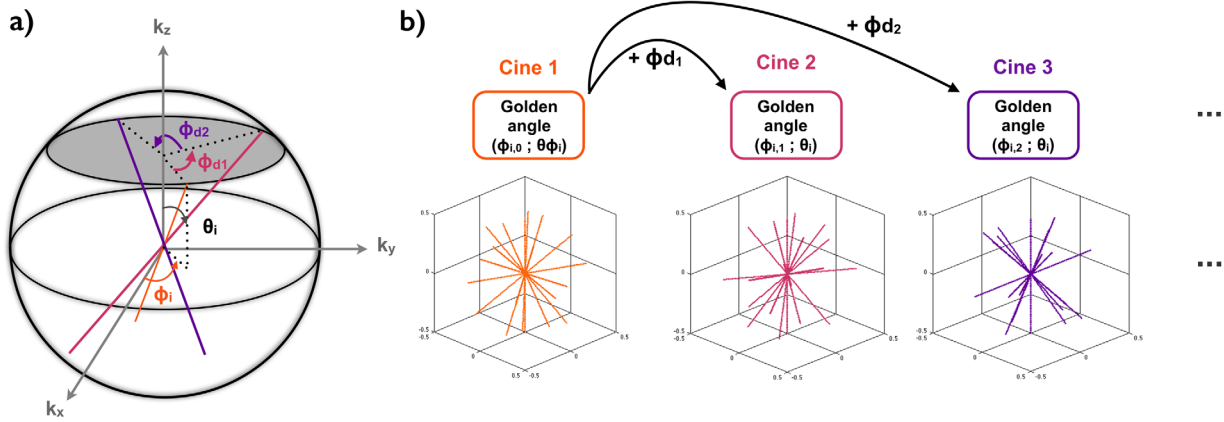


FIG. 2. Method used to insert a second golden angle between consecutive cine images. **(a)** The orange line represents the trajectory of a projection defined by the first golden angle, corresponding to cine image 1. For cine image 2 (pink), the new trajectory was defined by adding Φ_{d1} . For cine image 3 (purple), an increment of Φ_{d2} was introduced. The same value, θ_i , was used between adjacent cine projections. **(b)** Example of how nine projections are distributed for three consecutive cine images.

$$\Phi_{d_j} = 2\pi \times \text{mod}(v_2 \times j) \quad [6]$$

where $v_2 = 0.4656$ radians was previously defined.

This additional angle results in a similar k-space sampling distribution between cines, but different k-space sampling trajectories (Fig. 2). These can then be combined to increase the resolution of each cine image, as shown in Figure 3.

Reconstruction procedure

To reconstruct a frame volume at a specific time, a temporal filter was applied to each cine with an aperture in the radial direction depending on the time separating the reconstructed and surrounding cine. In the reconstructions performed for this article, the filter was defined by two parameters, Q and R ($Q \leq R$). Q corresponds to the cine number where one-half of the higher frequencies from ech-

oes were used and $(R-Q)$ refers to the cine number where one-quarter of the higher frequencies from echoes were used, as shown in Figure 3a,b. In this figure, reconstruction was performed using samples of projection with a ($Q=1$, $R=3$) filter. Using the definition of Haider et al. (36), this corresponds to a temporal footprint of $TR \times 7$. Blue and orange samples were used to reconstruct the outer part of the sphere (high frequencies); red and dark purple samples were used for the middle of the sphere; and all light purple samples were used because they defined the temporal resolution of the images to be reconstructed.

K-space data were regridded with an oversampling ratio of 2 using a Kaiser-Bessel kernel (37). Data were also transformed by applying a conventional fast Fourier transform (FFT). Each phased array receiver magnitude image was reconstructed using the method described above, and then combined by a sum of squares reconstruction.

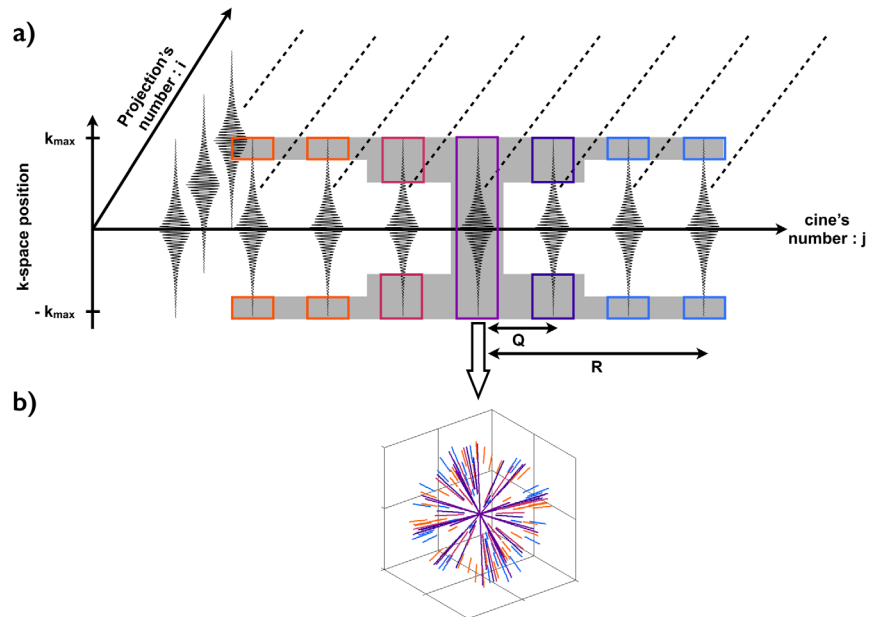


FIG. 3. Temporal filter scheme (gray) used to reconstruct cine image 5. **(a)** Data were reconstructed using one-half of the high projection frequencies from echoes generated at a Q time distance, and one-quarter from echoes at a greater time distance (from Q to R). **(b)** Schematic representation of the k-space for cine image 5 after applying this temporal filter.

Experiments

Magnet and gradient system

Experiments were performed on a 7-Tesla Bruker Biospec (Ettlingen, Germany) equipped with a gradient system capable of 660 mT/m maximum strength and 110 μ s rise time. A volume resonator (75.4 mm inner diameter, active length = 70 mm) operating in quadrature mode was used for excitation, and a four-element (2×2) phased array surface coil (outer dimensions of one coil element: 12×16 mm²; total outer dimensions: 26×21 mm²) was used for signal reception.

Animal preparation

All experimental procedures were approved by the Animal Care and Use Institutional Ethics committee of Bordeaux, France (Approval No. 5012032-A).

Mice (C57/black 6; $n = 12$; body weight 22–27 g) were anesthetized with isoflurane (1.0% in air). The ECG signal was picked up using electrodes wrapped around the forelimbs. This signal was converted into a square trigger pulse by a specific monitoring and gating system (SA Instruments, Inc., NY) connected to the spectrometer. A respiratory sensor was placed under the animal's thorax. ECG and respiratory signals were visualized on a user interface; cardiac rhythm was stabilized (425–475 beats/min); and anesthesia was regulated by modifying the isoflurane percentage inhaled.

Carotid artery ligation

Mice ($N = 4$) were anesthetized with isoflurane in air at 4% during induction and at 1.5% during surgery. Xylocaine was injected directly into the trachea before making a midline neck incision. An 8-0 polypropylene monofilament suture (Ethicon Inc., Somerville, NJ) was used to ligate the right common carotid artery 1 cm above the aortic arch. The surgical wound was sutured and animals underwent imaging 3 days after the surgery.

MRI Parameters

Anatomical radial time-of-flight imaging

Images were acquired on mice placed supine into the magnet with a 3D, slice selective, golden angle radial sequence with the following parameters: echo time/repetition time (TE/TR) = 2.5/5.5 ms; excitation pulse: sinc10H = 400 μ s; flip angle = 15°; slice thickness = 15 mm; axial orientation, bandwidth (BW) = 100 kHz; field of view (FOV): $20 \times 20 \times 20$ mm; matrix: $192 \times 192 \times 192$; spatial resolution = $(104 \mu\text{m})^3$. Images were acquired with 40,000 projections (2 min 40 sec total acquisition time)—and the first 8,000, 4,000, and 2,500 projections were used to reconstruct undersampled images corresponding to an acquisition time of 44 sec, 22 sec, and 13.75 sec, respectively.

Time-resolved time-of-flight imaging

A suppression module was applied before a 3D-triggered slice selective N-cine double golden angle radial sequence to acquire 20 (carotid arteries studies) or 30 volumes

(Circle of Willis studies) composed of a maximum of $P = 8,000$ projections.

The suppression volume was placed at the same position as the imaging volume to initially suppress signal from both the stationary tissues and the moving spins, as illustrated in the chronogram (Fig. 1).

Phantom imaging

To determine how well the undersampled strategies estimate flow dynamics, experiments were performed on a custom-built phantom composed of both stationary spins in a cylinder and moving spins in a straight tube containing flowing water. The diameter of this tube was 0.5 mm; and a flow rate of 3.75 mL/min was maintained corresponding to a mean velocity of 31.8 cm/s. Experiments were performed with the following parameters: TE/TR = 1.5/3.3 ms; $\alpha = 12^\circ$; bandwidth = 200 kHz; FOV: $25 \times 25 \times 25$; readout matrix = 192; resolution = $(130 \mu\text{m})^3$.

Blood flow in carotid arteries

Mice were positioned supine within the magnet with the neck at the center of the NMR coil. An ECG-triggered sequence was used with the following parameters: TE/TR = 1.5/3.3 ms; $\alpha = 12^\circ$; BW = 200 kHz; FOV: $25 \times 25 \times 25$; readout matrix = 192; resolution = $(130 \mu\text{m})^3$; and slice thickness = 20 mm. No saturation of venous blood signal was necessary, as previously described (31).

Blood flow in brain arteries

Mice were positioned prone within the magnet with the head at the center of the NMR coil. Images were acquired with a thickness of 10 mm inside a 25-mm FOV, and 30 cine images were acquired after applying the suppression module. Except for the slice thickness and cine images, the same parameters were used as for previous experiments. Images were compared for healthy mice and mice on which a ligation procedure had been performed on the right common carotid artery.

Quantitative Time-Resolved Image Analysis

Volume as a function of time

For phantom and carotid time-resolved imaging, signals from moving spins were binarized for each cine image: 1 for values greater than (maximum signal)/(standard deviation (std)(Noise) $\times 3$) and 0 for lower values.

The number of voxels for each cine image was multiplied by the voxel size and is reported as a function of time.

Signal-to-noise ratio and intensity profile

Axial images of the carotid artery after its emergence from the aortic arch were analyzed. The number of pixels in each of the horizontal and vertical dimensions was increased from 192 pixels to 2,880 pixels by bilinear interpolation. The signal-to-noise ratio (SNR) was measured based on regions of interest on the carotid and the outer void. An intensity profile was reported for the carotid artery as a function of the number of projections and with or without the use of temporal filter.

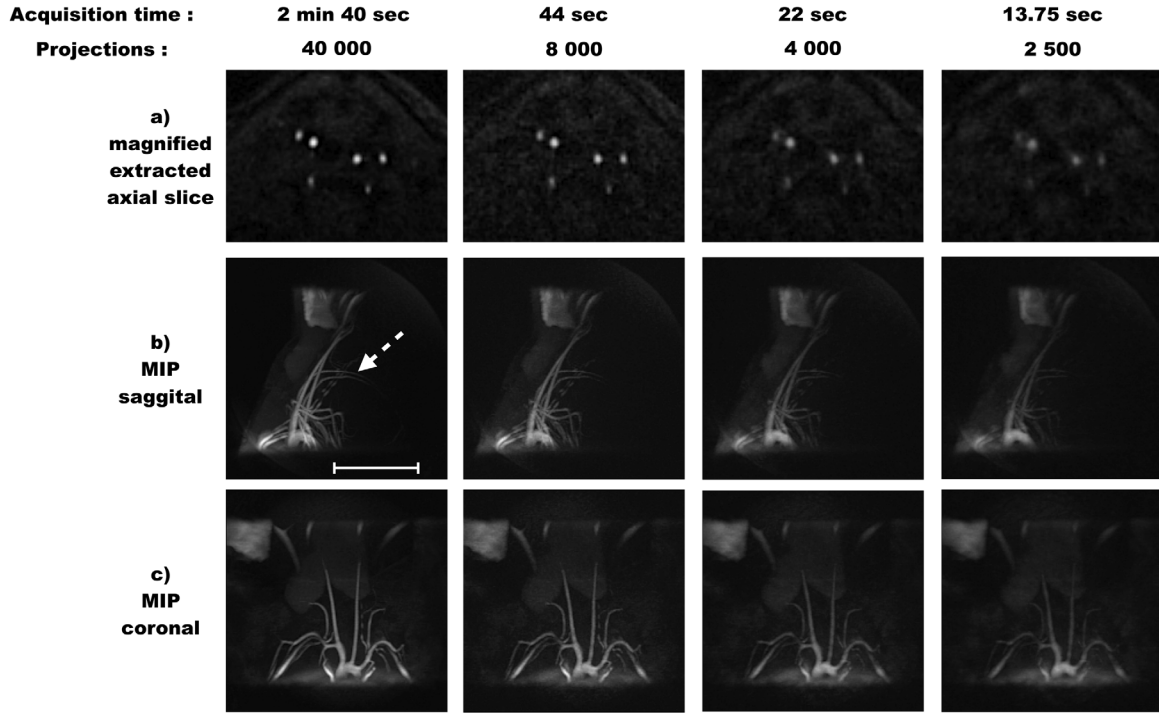


FIG. 4. Anatomical radial magnetic resonance angiography (MRA) images at the aortic arch and carotid levels in mice. Radial MRA was obtained with 40,000, 8,000, 4,000, and 2,500 projections (as defined by the golden angle ratio). **(a)** Magnified extracted axial slice through the carotid arteries. **(b)** Sagittal maximum intensity projection (MIP) views. **(c)** Coronal MIP views. Dashed arrow indicates axillary arteries. Scale bar represents 10 mm.

Estimation of point spread function

The point spread function (PSF) was estimated by substituting one for raw data values and gridding them using the procedure described above. Two different trajectories were used: the time-resolved golden angle trajectory defined previously; and a method explained by Saff et al. (38), which distributes many points uniformly over a sphere with the same Φ_d angle between cine phases—as in the time-resolved golden angle trajectory. The full width at half maximum (FWHM) for the PSF was measured on cine number 10 for a reconstruction of 20 cine volumes. Cine volumes were reconstructed using 4,000, 2,500 and 1,000 projections with and without a ($R=3$, $Q=1$) temporal filter in both cases.

Flow image representation

Data was reconstructed such that the signal in voxels was proportional to the total time of flow presence in each voxel. All cine volumes were binarized with the same fixed value and then added to form a single volume (39). A jet-black color map was applied to maximum intensity projection (MIP) images of brain arteries. The red to blue color code corresponds to a visualization of blood from the start to the end of cine images.

RESULTS

Anatomical Time-of-Flight Angiography of Murine Carotid

Radial data were reconstructed with decreasing numbers of projections: 40,000 (2 min 40 sec), 8,000 (44 sec), 4,000 (22 sec), and 2,500 (13.75 sec). Figures 4a, 4b, and

4c show a representative magnified axial view and representative sagittal and coronal MIP views, respectively. Signals corresponding to moving spins are readily visible in the major arteries (aortic arch, carotid, jugular and vertebral arteries) in all images. The SNR measured on the left carotid (Fig. 4a) was 88.8 ± 0.4 , 57.1 ± 0.2 , 52.8 ± 2.7 , and 54.8 ± 0.3 for 40,000, 8,000, 4,000, and 2,500 radial images, respectively.

As observed in Cartesian imaging, an attenuation of blood signal can occur for distal arteries (dashed arrow).

The major effect of undersampling was visible for spatial resolution (Fig. 4a). On images with only 2,500 projections, significant blurring was observed, making the vessels difficult to distinguish. However, the complete angiogram was well-defined on images obtained with just 4,000 projections over an acquisition time of 22 seconds.

Time-Resolved Imaging

Point spread function measurements

As reported in Table 1, for the nonfiltered 3D golden angle reconstruction and 4,000 projections, FWHM was equal to 1.996 ± 0.022 pixels, whereas for the uniform distribution it was 1.985 ± 0.039 pixels. With the temporal filter ($R=3$, $Q=1$), FWHM dropped to 1.458 ± 0.044 pixels and 1.471 ± 0.007 pixels, respectively. This suggests that the filtered reconstruction improved resolution. Furthermore, the 3D golden angle approach provided a slightly higher image resolution than did the uniform sample distribution for this value of undersampling factor. Decreasing the number of projections

Table 1
Point Spread Function Estimation in Pixels on a Cine Data Acquired with a Double Golden Angle Trajectory or a Standard Radial Trajectory. **Texte**

Number of Projections	Golden Angle Trajectory		Standard Radial Trajectory	
	unfiltered	filtered ($R=3$, $Q=1$)	unfiltered	filtered ($R=3$, $Q=1$)
1,000	2.173 ± 0.012	1.497 ± 0.035	2.208 ± 0.019	1.487 ± 0.021
2,500	2.085 ± 0.004	1.479 ± 0.035	2.065 ± 0.062	1.482 ± 0.041
4,000	1.996 ± 0.022	1.458 ± 0.044	1.985 ± 0.039	1.471 ± 0.007

Data are listed according to the number of projections and whether a temporal filter was applied.

increased the FWHM. Nevertheless, this value were in the range of 1.48 using the temporal filter.

Phantom imaging

Images of moving spins in a straight tube were reconstructed with 8,000 (data not shown) radial projections, 4,000 (TA=4 min 51 s) radial projections, or 1,000 (TA=1 min 13 s) radial projections without applying the temporal filter, and with 1,000 projections with the temporal filter ($Q=1$, $R=3$). Coronal MIP images are presented in Figure 5a, 5b, and 5c. Figure 5 (last column) presents the tube profile after signal saturation at the level of the dashed line illustrated on the image for $t=21.94$ ms on Figure 5a. On 4,000-projection cine images, water flow through the FOV was easily visualized, and its flow rate could be accurately measured (the peak velocity was equal to 65 cm/s, corresponding to twice the mean velocity). A similar value was obtained with 8,000 radial projections. As expected, with only 1,000 projections both signal and spatial resolution were affected. Signal from the tube decreased from 10 to 4.2 with 4,000 and 1,000 projections, respectively. Once again, critical streaking artifacts were present, which pre-

vented accurate measurement of flow velocity (arrow, Fig. 5b). Reconstruction with a ($Q=1$, $R=3$) filter suppressed most of the streaking artifacts on 1,000-projection images (Fig. 5c). Furthermore, the tube signal profile with 1,000-projection reconstruction increased from 4.2 to 8 when the filter was applied; thus, it became similar to the profile obtained with 4,000 projections.

Moving spin volumes within the FOV were measured over time during all cine phases (data not shown). Image reconstructions combined with the temporal filter had no influence on the volume and flow rate measured with 4,000 projections. In contrast, volumes were overestimated with 1,000 projections because of the presence of streaking artifacts and the lower spatial resolution.

In vivo experiments: carotid arteries imaging

Coronal and sagittal MIP views of time-resolved TOF images were obtained on carotid arteries in healthy mice (Supp. Fig. 1). The images shown were obtained with 4,000 projections and a reconstruction filter ($Q=1$, $R=3$). The high temporal and spatial resolutions made it possible to follow the blood flowing into the carotids and then into subarteries during systole.

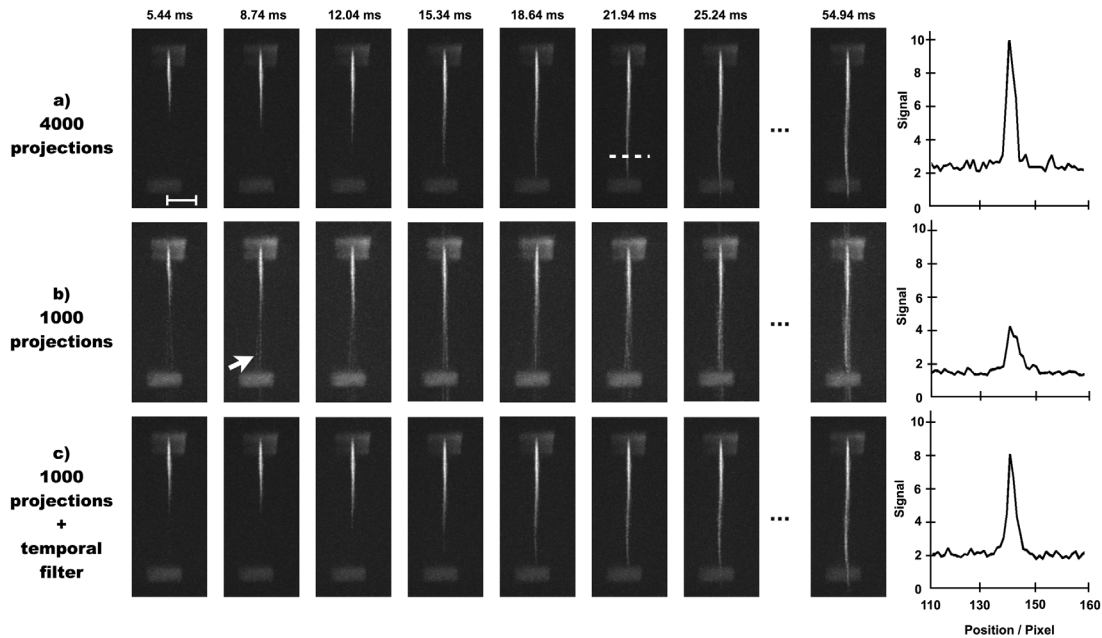
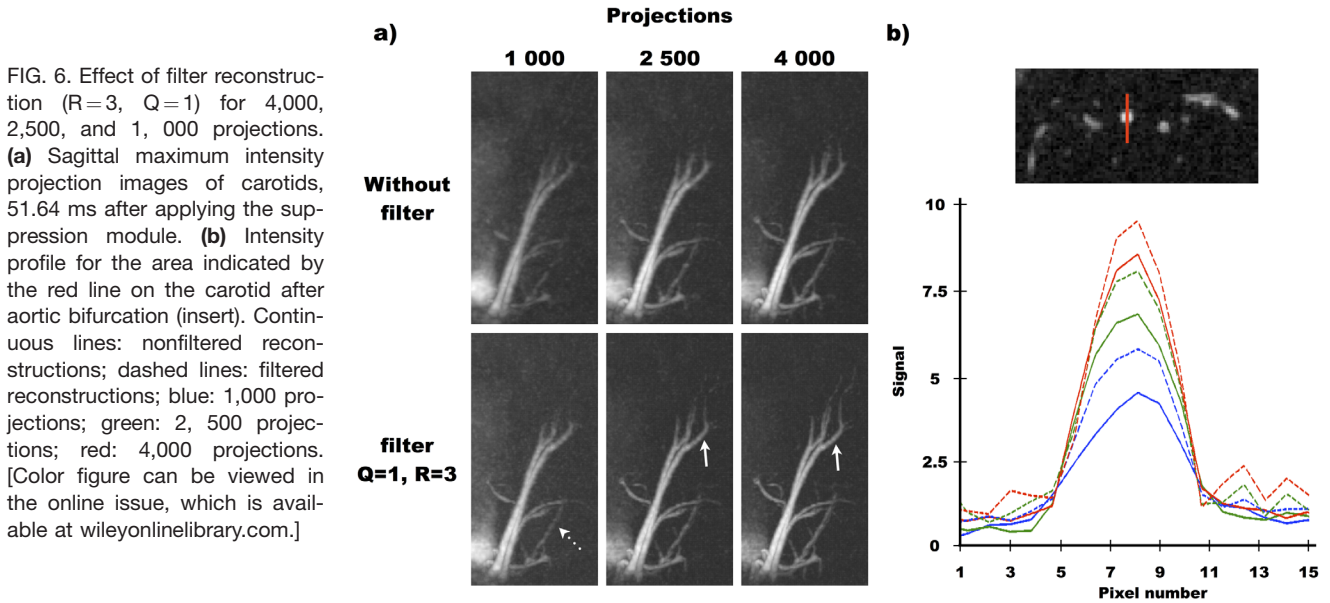


FIG. 5. Coronal maximum intensity projection of the time-resolved sequence on the flow phantom. Comparison between images acquired with (a) 4,000 or (b) 1,000 projections, and (c) 1,000 projections reconstructed after applying a filter ($R=3$, $Q=1$). Scale bar represents 5 mm. The intensity profile at the level of the dashed line is shown for each reconstruction in the last column.



To assess the impact of the temporal filter on image reconstruction, a vessel intensity profile was generated (Fig. 6). Compared to unfiltered images, filtered images appeared less blurry, resulting in the better detection of smaller vessels (dashed arrow, Fig. 6a). Spatial resolution was clearly enhanced when using the filter, as shown by the better delineation of the left internal and external carotids (arrow head). Filtered data from 4,000 and 2,500 projections produced images of similar quality. With only 1,000 projections and filtered reconstruction, major arteries were still well defined.

The carotid signal (Fig. 6b) was measured on images acquired with and without a filter. SNR is presented in Table 2. This data shows that the SNR increased with the number of projections used for reconstruction when no filter was applied. However, the SNR was slightly lower with filtered measurements.

Blood volumes were measured as a function of time and compared (Fig. 7). Flow rates, measured between 5 ms and 20 ms—which correspond to the systole phase—were similar for all the reconstructions. However, the flow rate was underestimated when measured on 1,000-projection unfiltered images. After 20 ms, the blood volumes were overestimated with 1,000, 1,000 + filter, and 2,500 projections compared to those measured with 2,500 + filter, 4,000, and 4,000 + filter.

Table 2
SNR Was Measured on an Axial View of the Carotid Generated by Time-Resolved Imaging (Fig. 6)

Number of Projections	SNR	
	unfiltered	filtered (R = 3, Q = 1)
1,000	31.41 ± 2.11	31.52 ± 0.59
2,500	38.92 ± 1.53	36.42 ± 3.03
4,000	39.35 ± 6.01	36.15 ± 1.80

Data are listed according to the number of projections and whether a temporal filter was applied.

In vivo experiments: Circle of Willis imaging

Sixteen coronal MIP cine images were extracted from the 30 images acquired for a representative healthy mouse (Fig. 8a) and compared to a mouse with a ligated left carotid (Fig. 8b). These ECG-triggered images were obtained with 2,500 projections and filter over a total acquisition time of 5 min.

The high temporal resolution of the cine images made it possible to observe filling of the Circle of Willis in both experiments. In ligated mice, as in healthy mice, the whole circle was filled. However, because only the right carotid was functional in ligated animals, it took longer to fill the entire circle. This could be observed and quantified on a color map (Suppl. Fig. 2). With this representation, blood reached the position indicated by the white arrow approximately 30 ms after volume suppression in healthy mice (Suppl. Fig. 2a) compared to almost 70 ms in the ligated mice (Suppl. Fig. 2b).

Movies of cine images are available as Suppl. Videos 1 and 2.

DISCUSSION

This article demonstrates that single and double golden angle radial imaging approaches can be used to very efficiently compute either 3D undersampled anatomical images or time-resolved TOF angiography in mice, respectively.

A 3D radial encoding method is commonly used in dynamic contrast-enhanced (DCE) T1 imaging and in phase contrast imaging (23,26,40). However, we have found no reference to its use in classical TOF anatomical angiography in either humans or mice. In this article, a strong TOF effect was obtained with appropriate slice selection, that is, using a slice thinner than a radial FOV. As previously mentioned, radial imaging is more robust in determining motion and flow dephasing than is Cartesian imaging (data not shown). This explains how we were able to obtain a very homogeneous signal for the aortic arch despite movement due to respiration and fast,

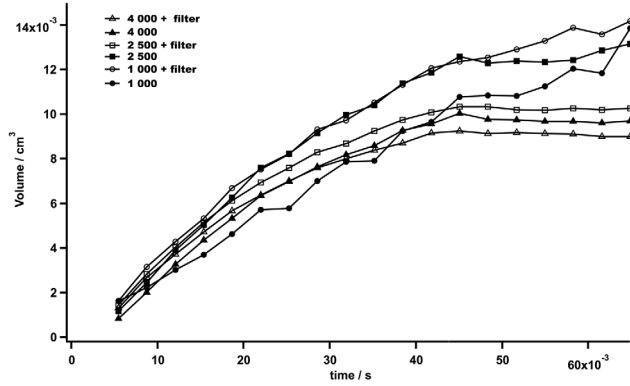


FIG. 7. Blood volume measured as a function of time after applying the suppression module to carotids from a healthy mouse. Data represented were measured with 4,000, 2,500, and 1,000 projections, with and without filter ($R=3$, $Q=1$) reconstruction.

turbulent blood flow. Radial imaging is also able to undersample the k-space. Indeed, in our study, acceptable image quality was obtained with only 4,000 projec-

tions, resulting in a 10-fold reduction in total acquisition time compared to our highly sampled data. The third advantage of the proposed method is due to the golden angle approach. With this strategy, an approximately uniform distribution of radial spokes can be obtained over time even with low numbers of projections. This can be very helpful when the necessary number of projections is not known in advance. Furthermore, if acquisition must be stopped before completion, a good quality image can nevertheless be reconstructed. This is not the case with conventional radial imaging using linearly ordered projections in which large areas of k-space would remain empty. Golden angle trajectories can be postprocessed using treatments such as self-gating, whereas with uniform radial trajectories removing corrupted projections can produce an empty zone within the k-space.

Thus, radial imaging using a golden angle approach can be very efficient for anatomical TOF imaging when the acquisition time needs to be limited and when motion-sensitive areas are of interest.

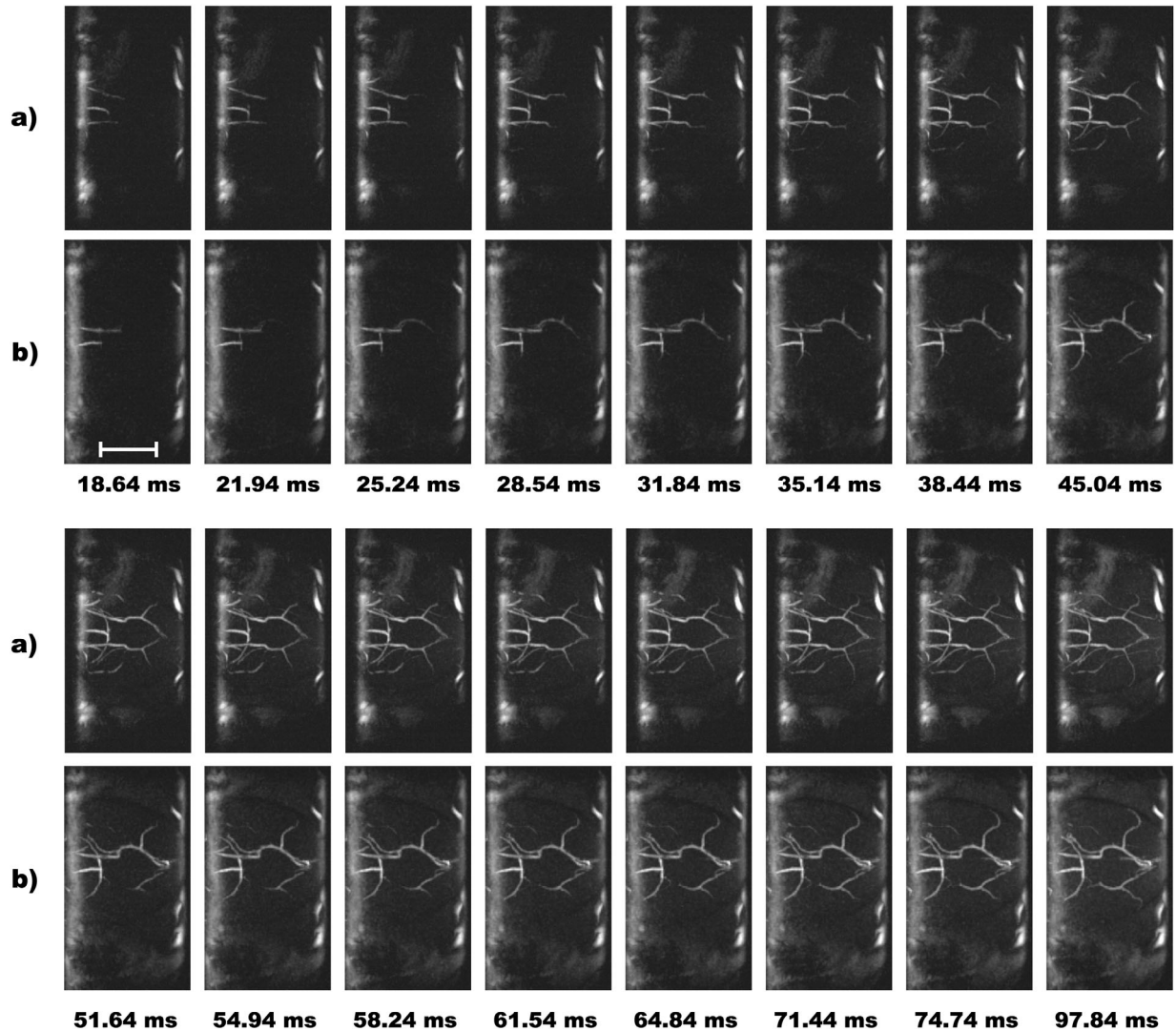


FIG. 8. Time-resolved coronal maximum intensity projection images for a healthy mouse (a) and for a mouse with a ligated carotid artery (b). Sixteen images were extracted from 30 cine images. Scale bar represents 5 mm.

This undersampled approach was then extended to time-resolved angiography to visualize blood flow with very high temporal resolution while maintaining a limited acquisition time. Our results showed that flow imaging in carotid and brain arteries with an adequate SNR could be obtained with a 3.3 ms temporal resolution. This resolution provided excellent details on the flow dynamics; it also provided accurate measurement of blood velocity thanks to the increased number of cine images that could be generated between two R-waves. The possibility of considerably reducing the total acquisition time with the radial method compared to other nonenhanced time-resolved angiography is an advantage for flow measurement. Indeed, to generate such spatial and temporal resolutions using Cartesian trajectories, at least 2 or 3 averages would be needed for SNR and sensitivity to motion reasons, which would increase the total acquisition time and decrease the effective temporal resolution. An echo planar imaging approach could be used to reduce the acquisition time with Cartesian imaging, but temporal resolution is limited due to the length of the echo train, and spatial resolution is also affected by distortion artifacts—particularly at high magnetic field. Other non-TOF-based imaging techniques are also widely used, but these are generally time-consuming. On humans, dynamic MR angiography with spin labeling techniques [Signal Targeting with Alternating Radiofrequency (STAR) (41), STAR and Flow-Independent Relaxation Enhancement (STARFIRE) (42), true fast imaging with steady-state precession -based spin tagging with alternating radiofrequency (TrueSTAR) (43)] requires two acquisitions before complex subtraction of selective and nonselective inversion recovery images can be performed. Similarly, 3D phase contrast techniques can be effectively used to visualize dynamic blood flow, but at least four acquisitions are needed (44). In addition, this technique, although useful for large human vessels, has not been extensively used on small animals.

The main novelty of this article is the use of a double golden angle approach on 3D prospective acquisition. A single golden angle approach offers high flexibility in terms of spatial and temporal resolution, but is limited to retrospective acquisition in cardiac MRI (45) and in DCE-MRI. Very recently, Koktzoglou used a golden angle ratio between cine images within each heartbeat to reconstruct an arbitrary number of cardiac phases (46) using a standard spiral distribution over successive heartbeats. This reduces the number of postprocessing techniques that can be used—and produces less usable images if acquisition is interrupted.

Here, the double golden angle approach allowed us to use an efficient temporal filter to increase the spatial resolution of cine images. This method showed a very efficient distribution of projections within and between cine phases, as well as a low sensitivity to streaking artifacts. Filter-reconstructed images allowed us to visualize vessels of less than 300- μ m diameter with only a small number of projections. To reconstruct one cine-image at a defined time, parts of six neighbor frames were added to the central frame. This corresponded to a temporal footprint of 23.1 ms. Even if this value can appear long compared to native temporal resolution, it

did not seem to alter flow measurements because similar results were produced with data obtained from a large number of projections or from a low number of filtered projections. This is because only a part of the high spatial frequencies was used to create the temporal filter and the flow rate was low compared to the temporal resolution used here. In a case of a higher velocity, the temporal footprint would certainly have to be reduced. Due to the very high flexibility of this strategy, it is possible to reconstruct different temporal resolutions and to use different types of filter after image acquisition.

The main limitation of the method presented here is that it requires thinner selective slabs than does radial FOV. This is required to obtain a sufficient TOF effect on vessels with low flow velocities. This limitation decreases the potential of undersampled strategies compared to classic Cartesian imaging. This limitation would be particularly true for human studies in which very small size slabs compared to radial FOV have to be used. Nevertheless, anisotropic FOV (47) combined with a different golden angle approach could reduce the acquisition time to compensate for this drawback. Stack-of-stars encoding with thin slice selection (48) and the same double golden angle approach can also be an alternative for human studies.

Due to its versatility, the method could be further improved. In terms of spatial resolution, more sophisticated filters could be used (49). To further decrease the total acquisition time, this method could be combined with other acceleration approaches such as parallel imaging, compressed sensing, or constrained backprojection reconstruction. Indeed, compressed sensing is particularly appropriate for use with radial golden angle trajectories because of the high incoherence in multiple directions, which makes it possible to use sparsity (50). Constrained backprojection reconstruction (51) also takes advantage of the prospective golden angle approach; the nonrepetition of trajectories between cine phases makes it possible to reconstruct high-resolution images with all the projections. This strategy, combined with the double golden angle approach, could be more efficient for blood flow-triggered imaging because the time between the end of cine projections and the next R-waves can be used to acquire more projections, yielding a higher resolution composite image.

CONCLUSION

This study demonstrates that 3D radial TOF imaging is efficient for time-resolved blood flow imaging in small animals. This technique simultaneously provides high 3D isotropic spatial resolution and a temporal resolution of 3 ms with a good SNR, all of which are necessary for blood flow imaging. The double golden angle approach was also highly flexible. Although a constant temporal resolution was used, the method could be retrospectively adapted to reconstruct 3D prospective MRA acquisitions with any temporal and spatial resolution. This has important implications for time-resolved angiography in which flow velocities are not known before analysis, as well as for DCE cardiac cine MRI.

ACKNOWLEDGMENTS

This work was supported by a public grant, Translational Research and Advanced Imaging Laboratory, which is part of the French National Research Agency's Investments for the Future Program ("NewFISP"; ANR-10-LABX-57). The authors thank Stephane Sanchez for technical assistance.

REFERENCES

- Plump AS, Smith JD, Hayek T, et al. Severe hypercholesterolemia and atherosclerosis in apolipoprotein E-deficient mice created by homologous recombination in ES cells. *Cell* 1992;71:343–353.
- Eskandari MK, Vijungco JD, Flores A, Borensztajn J, Shively V, Pearce WH. Enhanced abdominal aortic aneurysm in TIMP-1-deficient mice. *J Surg Res* 2005;123:289–293.
- Chalothorn D, Zhang H, Clayton JA, Thomas SA, Faber JE. Catecholamines augment collateral vessel growth and angiogenesis in hind-limb ischemia. *Am J Physiol Heart Circ Physiol* 2005;289:H947–959.
- Kumar A, Lindner V. Remodeling with neointima formation in the mouse carotid artery after cessation of blood flow. *Arterioscler Thromb Vasc Biol* 1997;17:2238–2244.
- Jacoby C, Böring YC, Beck A, et al. Dynamic changes in murine vessel geometry assessed by high-resolution magnetic resonance angiography: a 9.4T study. *J Magn Reson Imaging* 2008;28:637–645.
- Beckmann N, Stirnimann R, Bochelen D. High-resolution magnetic resonance angiography of the mouse brain: application to murine focal cerebral ischemia models. *J Magn Reson* 1999;140:442–450.
- Beckmann N. High resolution magnetic resonance angiography non-invasively reveals mouse strain differences in the cerebrovascular anatomy in vivo. *Magn Reson Med* 2000;44:252–258.
- Krucker T, Schuler A, Meyer EP, Staufenbiel M, Beckmann N. Magnetic resonance angiography and vascular corrosion casting as tools in biomedical research: application to transgenic mice modeling Alzheimer's disease. *Neurol Res* 2004;26:507–516.
- Lefrançois W, Thiaudière E, Ben Hassen W, Sanchez S, Franconi J, Miraux S. Fast whole-body magnetic resonance angiography in mice. *Magn Reson Med* 2011;66:32–39.
- MacIntosh BJ, Sideso E, Donahue MJ, et al. Intracranial hemodynamics is altered by carotid artery disease and after endarterectomy: a dynamic magnetic resonance angiography study. *Stroke* 2011;42(4):979–984.
- Essig M, Engenhart R, Knopp MV, et al. Cerebral arteriovenous malformations: improved nidus demarcation by means of dynamic tagging MR-angiography. *Magn Reson Imaging* 1996;14:227–233.
- Wolf RL, Wang J, Detre JA, Zager EL, Hurst RW. Arteriovenous shunt visualization in arteriovenous malformations with arterial spin-labeling MR imaging. *AJNR Am J Neuroradiol* 2008;29:681–687.
- Mordini FE, Koktzoğlu I, Edelman RR. Time-resolved spin-labeled balanced steady-state free precession cineangiography for visualizing intracardiac shunt: technical considerations and clinical feasibility. *Magn Reson Med* 2012;68:1798–1806.
- Cochet H, Lefrançois W, Montaudon M, Laurent F, Pourtau L, Miraux S, Parzy E, Franconi J, Thiaudière E. Comprehensive phenotyping of salt-induced hypertensive heart disease in living mice using cardiac magnetic resonance. *Eur Radiol* 2013;23:332–338.
- De La Roque ED, Thiaudière E, Ducret T, et al. Effect of chronic hypoxia on pulmonary artery blood velocity in rats as assessed by electrocardiography-triggered three-dimensional time-resolved MR angiography. *NMR Biomed* 2011;24:225–230.
- Janiczek RL, Blackman BR, Roy RJ, Meyer CH, Acton ST, Epstein FH. Three-dimensional phase contrast angiography of the mouse aortic arch using spiral MRI. *Magn Reson Med* 2011;66:1382–1390.
- Bonnin P, Leger PL, Deroide N, et al. Impact of intracranial blood-flow redistribution on stroke size during ischemia-reperfusion in 7-day-old rats. *J Neurosci Methods* 2011;198:103–109.
- Nielsen YW, Thomsen HS. Contrast-enhanced peripheral MRA: technique and contrast agents. *Acta Radiol* 2012;53:769–777.
- Wright RC, Riederer SJ, Farzaneh F, Rossman PJ, Liu Y. Real-time MR fluoroscopic data acquisition and image reconstruction. *Magn Reson Med* 1989;12:407–415.
- Korosec FR, Frayne R, Grist TM, Mistretta CA. Time-resolved contrast-enhanced 3D MR angiography. *Magn Reson Med* 1996;36:345–351.
- Van Vaals JJ, Brummer ME, Dixon WT, et al. "Keyhole" method for accelerating imaging of contrast agent uptake. *J Magn Reson Imaging* 1993;3:671–675.
- Grist TM, Mistretta CA, Strother CM, Turski PA. Time-resolved angiography: past, present, and future. *J Magn Reson Imaging* 2012;36:1273–1286.
- Du J, Fain SB, Korosec FR, Grist TM, Mistretta CA. Time-resolved contrast-enhanced carotid imaging using undersampled projection reconstruction acquisition. *J Magn Reson Imaging* 2007;25:1093–1099.
- Wu Y, Chang W, Johnson KM, Velikina J, Rowley H, Mistretta C, Turski P. Fast whole-brain 4D contrast-enhanced MR angiography with velocity encoding using undersampled radial acquisition and highly constrained projection reconstruction: image-quality assessment in volunteer subjects. *AJNR Am J Neuroradiol* 2011;32:E47–E50.
- Lee GR, Seiberlich N, Sunshine JL, Carroll TJ, Griswold MA. Rapid time-resolved magnetic resonance angiography via a multiecho radial trajectory and GraDeS reconstruction. *Magn Reson Med* 2013;69:346–359.
- Wu Y, Kecskemeti SR, Johnson K, et al. HYPR TOF: time-resolved contrast-enhanced intracranial MR angiography using time-of-flight as the spatial constraint. *J Magn Reson Imaging* 2011;33:719–723.
- Kaewlai R, Abujudeh H. Nephrogenic systemic fibrosis. *AJR Am J Roentgenol* 2012;199:W17–W23.
- Robson PM, Dai W, Shankaranarayanan A, Rofsky NM, Alsop DC. Time-resolved vessel-selective digital subtraction MR angiography of the cerebral vasculature with arterial spin labeling. *Radiology*. 2010; 257:507–515.
- Wu H, Block WF, Turski PA, Mistretta CA, Johnson KM. Noncontrast-enhanced three-dimensional (3D) intracranial MR angiography using pseudocontinuous arterial spin labeling and accelerated 3D radial acquisition. *Magn Reson Med* 2013;69:708–715.
- Yan L, Wang S, Zhuo Y, et al. Unenhanced dynamic MR angiography: high spatial and temporal resolution by using true FISP-based spin tagging with alternating radiofrequency. *Radiology* 2010;256:270–279.
- Miraux S, Franconi J, Thiaudière E. Blood velocity assessment using 3D bright-blood time-resolved magnetic resonance angiography. *Magn Reson Med* 2006;56:469–473.
- Parzy E, Miraux S, Franconi J, Thiaudière E. In vivo quantification of blood velocity in mouse carotid and pulmonary arteries by ECG-triggered 3D time-resolved magnetic resonance angiography. *NMR Biomed* 2009;22:532–537.
- Cochet H, Montaudon M, Laurent F, Calmettes G, Franconi J, Miraux S, Thiaudière E, Parzy E. In vivo MR angiography and velocity measurement in mice coronary arteries at 9.4 T: assessment of coronary flow velocity reserve. *Radiology* 2010;254:441–448.
- Barger AV, Block WF, Toropov Y, Grist TM, Mistretta CA. Time-resolved contrast-enhanced imaging with isotropic resolution and broad coverage using an undersampled 3D projection trajectory. *Magn Reson Med* 2002;48:297–305.
- Chan RW, Ramsay EA, Cunningham CH, Plewes DB. Temporal stability of adaptive 3D radial MRI using multidimensional golden means. *Magn Reson Med* 2009;61:354–363.
- Haider CR, Hu HH, Campeau NG, Huston J 3rd, Riederer SJ. 3D high temporal and spatial resolution contrast-enhanced MR angiography of the whole brain. *Magn Reson Med* 2008;60:749–760.
- Beatty PJ, Nishimura DG, Pauly JM. Rapid gridding reconstruction with a minimal oversampling ratio. *IEEE Trans Med Imaging* 2005;24:799–808.
- Saff EB, Kuijlaars ABJ. Distributing many points on a sphere. *Math Intell* 1997;19:5–11.
- Sallustio F, Kern R, Günther M, et al. Assessment of intracranial collateral flow by using dynamic arterial spin labeling MRA and transcranial color-coded duplex ultrasound. *Stroke* 2008;39:1894–1897.
- Hulet JP, Greiser A, Mendes JK, McGann C, Treiman G, Parker DL. Highly accelerated cardiac cine phase-contrast MRI using an undersampled radial acquisition and temporally constrained reconstruction. *J Magn Reson Imaging* 2013. doi: 10.1002/jmri.23310.
- Gai ND, Talagala SL, Butman JA. Whole-brain cerebral blood flow mapping using 3D echo planar imaging and pulsed arterial tagging. *J Magn Reson Imaging* 2011;33:287–295.

42. Koktzoglou I, Edelman RR. STAR and STARFIRE for flow-dependent and flow-independent noncontrast carotid angiography. *Magn Reson Med* 2009;61:117–224.
43. Yan L, Wang S, Zhuo Y, et al. Unenhanced dynamic MR angiography: high spatial and temporal resolution by using true FISP-based spin tagging with alternating radiofrequency. *Radiology* 2010;256:270–279.
44. Johnson KM, Markl M. Improved SNR in phase contrast velocimetry with five-point balanced flow encoding. *Magn Reson Med* 2010;63:349–355.
45. Hansen MS, Sørensen TS, Arai AE, Kellman P. Retrospective reconstruction of high temporal resolution cine images from real-time MRI using iterative motion correction. *Magn Reson Med* 2012;68:741–750.
46. Koktzoglou I. 4D Dark blood arterial wall magnetic resonance imaging: methodology and demonstration in the carotid arteries. *Magn Reson Med* 2013;69:956–965.
47. Larson PZ, Gurney PT, Nishimura DG. Anisotropic field-of-views in radial imaging. *IEEE Trans Med Imaging* 2008;27:47–57.
48. Kecskemeti S, Johnson K, Wu Y, Mistretta C, Turski P, Wieben O. High resolution three-dimensional cine phase contrast MRI of small intracranial aneurysms using a stack of stars k-space trajectory. *J Magn Reson Imaging* 2012;35:518–527.
49. Lin W, Guo J, Rosen MA, Song HK. Respiratory motion-compensated radial dynamic contrast-enhanced (DCE)-MRI of chest and abdominal lesions. *Magn Reson Med* 2008;60:1135–1146.
50. Chan RW, Ramsay EA, Cheung EY, Plewes DB. The influence of radial undersampling schemes on compressed sensing reconstruction in breast MRI. *Magn Reson Med* 2012;67:363–377.
51. Mistretta CA, Wieben O, Velikina J, et al. Highly constrained back-projection for time-resolved MRI. *Magn Reson Med* 2006;55:30–40.